Operating regimes and contact resistance of side-bonded contacts to thin heavily doped semiconductor nanowires

Anvar Abdul Shukkoor, and Shreepad Karmalkar

Citation: Journal of Applied Physics **124**, 184502 (2018); doi: 10.1063/1.5053890
View online: https://doi.org/10.1063/1.5053890
View Table of Contents: http://aip.scitation.org/toc/jap/124/18
Published by the American Institute of Physics

Articles you may be interested in

Effects of nitrogen on the interface density of states distribution in 4H-SiC metal oxide semiconductor field effect transistors: Super-hyperfine interactions and near interface silicon vacancy energy levels
Journal of Applied Physics **124**, 184501 (2018); 10.1063/1.5045668

Space-charge and current non-uniformities, and contact resistivity of end-bonded metal contacts to thin heavily doped semiconductor nanowires
Journal of Applied Physics **124**, 084502 (2018); 10.1063/1.5041330

Effects of material degradation on electrical and optical characteristics of surface dielectric barrier discharge
Journal of Applied Physics **124**, 183301 (2018); 10.1063/1.5049463

Effect of $SrTiO_3$ oxygen vacancies on the conductivity of $LaTiO_3/SrTiO_3$ heterostructures
Journal of Applied Physics **124**, 185303 (2018); 10.1063/1.5046081

Transient analysis of luminescent coupling effects in multi-junction solar cells
Journal of Applied Physics **124**, 183103 (2018); 10.1063/1.5046543

Surface plasmon-enhanced near-field thermal rectification in graphene-based structures
Journal of Applied Physics **124**, 183104 (2018); 10.1063/1.5053162

Operating regimes and contact resistance of side-bonded contacts to thin heavily doped semiconductor nanowires

Anvar Abdul Shukkoor[a] and Shreepad Karmalkar[b]
Department of Electrical Engineering, Indian Institute of Technology, Madras, Chennai 600036, India

(Received 27 August 2018; accepted 24 October 2018; published online 13 November 2018)

In many nano-wire (NW) devices and during NW characterization, the contact is bonded on the surface or the *side* of the NW. The prior model of such *side-bonded* contacts assumes partial NW depletion and purely radial tunneling, both restricted to the contacted region. However, the real space-charge extends to the non-contacted NW, aided by the fringing field, and depletes the contacted NW fully for small NW radius, R. In addition, there are non-radial tunneling and generation-recombination near the contact edge. Supported by numerical calculations, the present work shows that when all the effects are included, different regimes of operation manifest in a side-bonded contact, and the space-charge and contact resistance can differ widely from prior predictions. Our calculations span contacts with barrier height, $\phi_{b0} = 0.4$–0.8 V on n-type silicon NWs of $R = 7.5$–20 nm and doping $N_d = 10^{18}$–10^{20} cm^{-3} and include the effects of dielectric confinement, NW length, surface defects, image force barrier lowering, and heavy doping. We find that a *side-bonded* contact gets fully depleted at the contact edge for $N_d \leq \alpha_{FD}[4\varepsilon_s\psi_0/qR^2]$, where ψ_0 = contact potential and $\alpha_{FD} = 0.73$ (0.88) for air (SiO_2) ambient. Furthermore, the behavior of a *side-bonded* contact approaches that of an *end-bonded* contact for $N_d \leq \alpha_{EB}[4\varepsilon_s\psi_0/qR^2]$, where $\alpha_{EB} = 0.16$ (0.30), while surface space-charge widths in the two contacts match over a much wider N_d range for SiO_2 ambient. We express the radial depletion width in the NW as an explicit function of the contact potential based on an available implicit relation. *Published by AIP Publishing.* https://doi.org/10.1063/1.5053890

I. INTRODUCTION

In nano-wire (NW) devices such as transistors and sensors, and during NW characterization, the contact metal can be bonded to either the *side* or the *end* of the NW[1] (see Fig. 1). The present paper deals with the operation of the side-bonded contact (SBC)[2–12] and shows that, under certain conditions, it behaves like an end-bonded contact (EBC) studied in the literature, e.g., see Refs. 13–18.

Prior studies[5,9–12] of SBCs estimate their contact resistance, R_C, based on the analytical Transmission Line Model (TLM). As per this model, the contacted NW is partially depleted and the depletion region is restricted to the contacted region; radially uniform current flows axially into the contacted NW; after entering the contacted region, the current decays over the transfer length as it tunnels radially into the contact [see Fig. 2(a)]. When NW radius, R, is small, the energy bands cannot bend much in the radial direction [see Fig. 2(b)], suppressing the radial tunneling and thereby raising R_C. This model has several limitations, since in reality:

- Band bending from the contact edge in the axial direction is large enough to move the NW conduction band close to the metal Fermi level [see Fig. 2(b)], causing edge tunneling [see Fig. 2(c)].
- The space-charge due to the contact potential extends into the non-contacted NW, aided by the fringing field [see Fig. 2(d)].
- NWs with small R, made possible by technological advance, get fully depleted beneath the contact [see Fig. 2(e)] at lower doping, N_d, or higher intrinsic contact barrier height, ϕ_{b0}.
- There is generation-recombination near the contact edge, since the effective lifetime, τ_N, in the NW is reduced by orders of magnitude below the bulk lifetime, τ_B, due to magnification of the surface recombination as per the formula[16] $\tau_N = (\tau_B^{-1} + 2s/R)^{-1}$, where s is the surface recombination velocity.

In this paper, we discuss the various operating regimes of an SBC arising from all the above effects. Furthermore, we calculate numerically space-charge widths and the current density associated with the contact and the R_C in these regimes and highlight conditions in which they differ significantly from those of the prior model. The calculations include the effects of dielectric confinement, NW length, surface defects, image force barrier lowering, and heavy doping. Using typical values from the recent literature, the contacts considered have the following parameter values: $\phi_{b0} = 0.4$–0.8 V spanning NiSi, TiSi, $ErSi_x$, $YbSi_x$, PtSi, Al, and Pt contacts[19–24] to n-type silicon NWs with R down to[25–27] 7.5 nm and doping[26,28,29] $N_d = 10^{18}$–10^{20} cm^{-3} surrounded by air or SiO_2, at 300 K.

We discuss the operating regimes and current phenomena in Sec. II and the space-charge width, current density,

[a]E-mail: anvar9101987@gmail.com
[b]E-mail: karmal@ee.iitm.ac.in

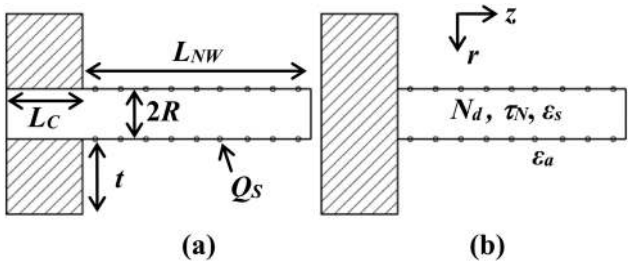

FIG. 1. (a) A side-bonded contact (SBC) and (b) the corresponding end-bonded contact (EBC) studied in this work. Hatched areas are metal contacts.

and R_C calculations in Sec. III and we summarize the limitations of the prior model in Sec. IV.

II. OPERATING REGIMES AND CURRENT PHENOMENA

The parameters of the SBC are R, N_d, ϕ_{b0}, and τ_N, defined above, and the surface charge Q_S, NW (ambient) permittivity ε_s (ε_a), NW length L_{NW} beyond the contact edge, and metal thickness t [see Fig. 1(a)]. We can identify the following three regimes of operation for the contact, based on its space-charge picture.

- *Partial depletion regime* [see Fig. 2(d)]: This occurs for high R, or high N_d, or low ϕ_{b0}. In this regime, the space-charge region is characterized by a radial width W_r under the contact and a fringing field dependent extension W_S along the NW surface beyond the contact edge. The prior model[5,9–12] treated this regime alone, that too neglecting W_S.
- *Full depletion regime* [see Fig. 2(e)]: This occurs for low R, or low N_d, or high ϕ_{b0}. In this regime, the space-charge region is characterized by, apart from W_S, a fringing field dependent extension W_A along the NW axis beyond the contact edge; note the radial non-uniformity of the space-charge edge reflected in $W_A < W_S$.
- *End bonded regime:* This is part of the full depletion regime, where a combination of low R, low N_d, and high ϕ_{b0} results in large W_A which drops a large part of contact potential ψ_0. Consequently, the radial potential variation over the NW cross section at the contact edge becomes small enough to make this cross section approximately equi-potential. This causes the *SBC* to behave as an *EBC* shown in Fig. 2(f).

The current in the above regimes can be due to tunneling or generation-recombination, denoted by I_T and I_{GR}, respectively, as discussed in our prior work[13,18] on EBC. The much higher space-charge width in a NW junction (as compared to a bulk junction) cuts down I_T but raises I_{GR}, which is further enhanced by the ultra low τ_N. The sum $(I_T + I_{GR})$ remains much higher than the thermionic emission, which can therefore be neglected. I_{GR} dominates at low N_d and high ϕ_{b0} for which space-charge widths are large, while I_T dominates elsewhere. Hence, we anticipate that I_{GR} will dominate in the low N_d part of the end-bonded regime of SBCs with small R and high ϕ_{b0}; I_T would dominate elsewhere. R_C will increase

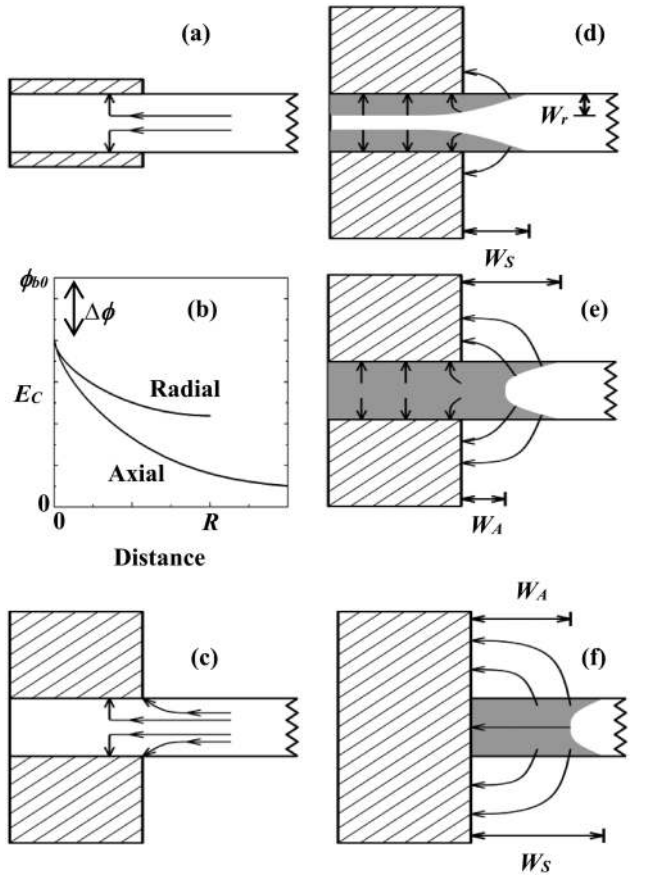

FIG. 2. (a) Current flow and metal electrode in the prior model of a side-bonded contact (SBC). (b) NW conduction band profile at the contact edge located at distance = 0, in the radial and axial directions; metal Fermi-level is at $E_c = 0$; $\Delta\phi$ represents image force barrier lowering. (c) Current flow (including the edge tunneling) and metal electrode in a real SBC. The space-charge and field lines in a partially depleted SBC (d), in a fully depleted SBC (e), and in an end-bonded contact (f).

with N_d in the I_{GR} dominated regime and decrease in the I_T dominated regime for the following reasons: (i) R_C is inversely proportional to the current and (ii) the space-charge width reduces as N_d is raised.

III. SPACE-CHARGE WIDTH, CURRENT, AND CONTACT RESISTANCE

For $R = 7.5$, 10, 20 nm, $\phi_{b0} = 0.4$, 0.8 V, and SiO_2 or air ambient, we calculated the space-charge widths W_r, W_A, and W_S, and the contact resistance R_C as a function of N_d in the range 10^{18}–10^{20} cm^{-3}. We also examined the impact of surface charge[30–32] $Q_S/q = \pm\ 3 \times 10^{11}$ cm^{-2} and the shortening of the NW to[5] $L_{NW} = 100$ nm on R_C. The trends discussed below have been derived from the resulting large number of calculations, out of which some representative ones are given in the paper for illustration. The parameter values common to all calculations are as follows: metal contact thickness $t = 350$ nm and length $L_C = 200$ nm (our results are unchanged for $t > 350$ nm); tunneling effective mass[21,33] $m = 0.3\ m_0$ and effective Richardson constant[19] $A^* = 270$ A cm^{-2} K^{-2} at $T = 300$ K. For GR calculations, based on measurements,[16] we chose $s = 2.5 \times 10^5$ cm/s leading to $\tau_N = 1.5$, 2, 4 ps for $R = 7.5$, 10, 20 nm.

Several publications[12,26,34,35] have established that the quantum confinement effects are negligible for $R \geq 7.5$ nm. On the other hand, random dopant fluctuation can be neglected and uniform doping assumed in a critical volume of the NW, if the number M of dopants in this volume is $\gg \sqrt{M}$, i.e.,$\sqrt{M} \gg 1$. The reason for this is as follows. It is known that[36] the semiconductor processing introduces the dopants in random locations such that the actual number of dopant atoms in a semiconductor volume can lie between the limits $M \pm \sqrt{M}$, where M is the average number. Let M denote the number of dopants in the space-charge region of our NW junction. Calculations for the smallest $R = 7.5$ nm yield $39 < M < 2262$, i.e., $6 < \sqrt{M} < 47$ for the range of N_d, ϕ_{b0}, and ambient dielectrics considered by us.

Since $\sqrt{M} \gg 1$, we are justified in assuming uniform doping in the space-charge region which governs the characteristics of the NW junction analyzed.

However, the dielectric confinement effects[26,37,38] and the heavy doping effects, namely, partial impurity ionization, impurity band formation, Fermi-Dirac statistics, and bandgap narrowing are relevant. Hence, our accurate calculations include these effects excluded in the prior model[5,9–12] with which our calculations are compared. Also, we derive an explicit equation for W_r in terms of ψ_0 using an available equation[10] which is implicit.

A. Calculation methodology

Device simulation softwares have proved quite effective for calculating characteristics of nanowire devices.[34,39] We used TCAD SENTAURUS software[40] for all these calculations. The 2D cylindrical Poisson's equation and electron continuity equation with drift-diffusion current were solved numerically, both inside and outside the NW. Electron and hole densities at the metal-NW junction were obtained on the basis of the thermionic emission-diffusion theory including image force barrier lowering. The non-local electron tunneling model was employed, where the tunneling from a point along the shortest path to the contact is represented as a net generation rate in the electron continuity equation. The details of these equations, boundary conditions, methodology, and calibration with measured data are identical to those we employed earlier to study EBC and are given in our previous work.[13,18] Further calibration of our SBC simulations is achieved by demonstrating the agreement of the simulated W_r with analytical calculations in Sec. II B, and the simulated current distributions with that of the prior model in Sec. II D. The prior model was implemented by utilizing the SENTAURUS software's option of simulating only the radial tunneling and turning off the fringing field by removing the surrounding dielectric.

B. Radial space-charge width

First, we discuss the derivation of the explicit equation for W_r in terms of ψ_0. Straightforward integration of Poisson's equation based on the depletion approximation of the space-charge leads to the following equation for ψ_0 in terms of W_r (e.g., see Ref. 10)

$$\psi_0 = \frac{qN_d}{2\varepsilon_s}\left[\frac{R^2 - (R - W_r)^2}{2} - (R - W_r)^2 \ln\left(\frac{R}{R - W_r}\right)\right]. \quad (1)$$

We cast this equation in a normalized form in terms of the normalized potential $u = (qN_dR^2/4\varepsilon_s)/\psi_0$ and the normalized depletion width $y = W_r/R$ as

$$u^{-1} = 1 + (1 - y)^2\left[\ln(1 - y)^2 - 1\right], \quad (2)$$

where $qN_dR^2/4\varepsilon_s$ is the radial potential drop from the contact to NW center, under the depletion approximation, in a fully depleted NW so that $0 \leq y \leq 1$ and $u \geq 1$. Rewrite the above as

$$\frac{u^{-1} - 1}{e} = \ln\left[\frac{(1 - y)^2}{e}\right] \exp\left\{\ln\left[\frac{(1 - y)^2}{e}\right]\right\}. \quad (3)$$

Considering that Lambert's W function[41] $z = W(x)$ is defined as the solution of the equation $x = z\ e^z$, the solution of the above equation can be written as

$$\ln\left[\frac{(1 - y)^2}{e}\right] = W\left(\frac{u^{-1} - 1}{e}\right). \quad (4)$$

Since $0 \leq y \leq 1$, we have $(1 - y)^2 \leq 1$ and so, LHS of the above equation is ≤ -1; hence, we employ the W_{-1} branch of Lambert's W function, and using $e^z = x/z$, solve for y from Eq. (4) as

$$y = 1 - \sqrt{(u^{-1} - 1)/W_{-1}\left(\frac{u^{-1} - 1}{e}\right)}, \quad (5)$$

where the term in the square root represents the undepleted NW region.

Figure 3(a) compares the results of Eq. (5) with those of our numerical calculations, where we take W_r as the radial distance from the contact where the space-charge falls to 50% of its peak [see Fig. 3(b)]. The normalized form of Eq. (5) enables a compact representation of results for a wide range of N_d, R, and ϕ_{b0}. A good match is seen for $W_r/R \leq 0.75$, confirming the soundness of our numerical calculations. However, for $W_r/R > 0.75$, at a given W_r, the numerically calculated

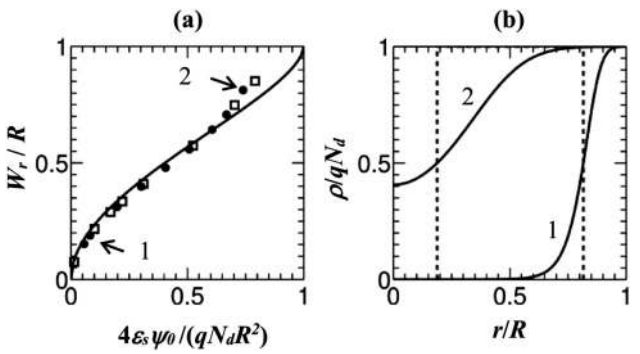

FIG. 3. (a) Normalized radial depletion width as a function of normalized contact potential. Lines represent Eq. (5) and points represent numerical calculations. (b) Radial distribution of the normalized space-charge corresponding to points 1 and 2 shown in (a). The solid line is numerical calculations and the dashed line is the depletion approximation. NW axis is at $r = 0$.

ψ_0 is seen to be less than the analytically calculated one. The reason for this can be traced with the help of Fig. 3(b), where the solid curve is the numerically calculated space-charge distribution and the dashed curve is its depletion approximation; $W_r/R \leq 0.75$ for curve 1 and $W_r/R > 0.75$ for curve 2. The potential is related to the area under the space-charge profile. Hence, the ψ_0 across the solid and dashed curves can be compared based on the former's tail on either side of the latter. It is evident from such a comparison that the ψ_0 across the solid and dashed curve 1 would be close, but the ψ_0 across solid curve 2 would be less than that across the dashed curve 2.

Due to the above consequences of the tail in the actual space-charge distribution, ψ_0 required to fully deplete a NW contact by a purely radial field is $< qN_dR^2/4\varepsilon_s$ predicted by the depletion approximation. In fact, extrapolation of the numerical results in Fig. 3(b) shows that a purely radial field depletes the contact fully for $N_d \leq 1.15[4\varepsilon_s\psi_0/qR^2]$. This condition holds at the left edge of the contact [see Fig. 2(d)]. At the right edge, however, the field is non-radial and higher due to the curvature of the space-charge edge [see Fig. 2(d)]. This results in less W_r for a given potential drop or $W_r = R$ (full depletion) at a lower N_d. Hence, the N_d required to fully deplete the NW at the right edge and hence all along the contact length is given by $N_d \leq \alpha_{FD}[4\varepsilon_s\psi_0/qR^2]$, where α_{FD} turns out to be significantly less than 1.15 as explained below.

C. Surface and axial space-charge widths

Figure 4 gives the W_S and W_A derived as the axial distance from the right contact edge where the equilibrium space-charge falls to 50% of its peak. Careful observation of all these plots reveals that as N_d is raised, W_A drops toward zero rapidly, i.e., the right edge of the contact enters the partial depletion regime, for $N_d > \alpha_{FD}[4\varepsilon_s\psi_0/qR^2]$, where the empirical constant $\alpha_{FDair} = 0.73$ within 16% error and $\alpha_{FDoxide} = 0.88$ within 12% error. We have $\alpha_{FDoxide} > \alpha_{FDair}$ because W_S is more and the space-charge edge curvature is less in SiO_2 in which the fringing field is stronger than that in air.

On the other hand, as N_d is reduced in the full depletion regime, W_A and W_S of the SBC increase and approach those of the EBC within 14% for $W_A \geq 1.5R$. This signifies entry of the contact into end-bonded regime. The simple intuitive condition $W_A \geq 1.5R$ translates to $N_d \leq \alpha_{EB}[4\varepsilon_s\psi_0/qR^2]$ empirically, where $\alpha_{EBair} = 0.16$ and $\alpha_{EBoxide} = 0.30$. We have $\alpha_{EBoxide} > \alpha_{EBair}$ since the stronger fringing field in SiO_2 enables achievement of the required $W_A = 1.5R$ at a higher N_d than in air. It is noteworthy that for SiO_2 (air) ambient, W_S versus N_d behavior of the SBC follows that of the EBC within 20% (40%) even beyond the end-bonded regime, the difference being maximum at $N_d = 1 \times 10^{20}$ cm^{-3}.

D. Contact resistance of contacts with long NWs

Consider the region $N_d \leq 3 \times 10^{18}$ cm^{-3} in high $\phi_{b0} = 0.8$ V contacts, where R_C increases for $R = 7.5$ nm (SiO_2) and decreases slowly for $R = 7.5$ nm (air) and for $R = 10$ nm (SiO_2) [see Figs. 5(a)–5(c)]. We identify this region as GR dominated and all other decreasing R_C regions as tunneling dominated following the description of the R_C behavior provided in Sec. II.

The R_C values of a SBC match with those of EBC in the GR dominated portion of the end-bonded regime.

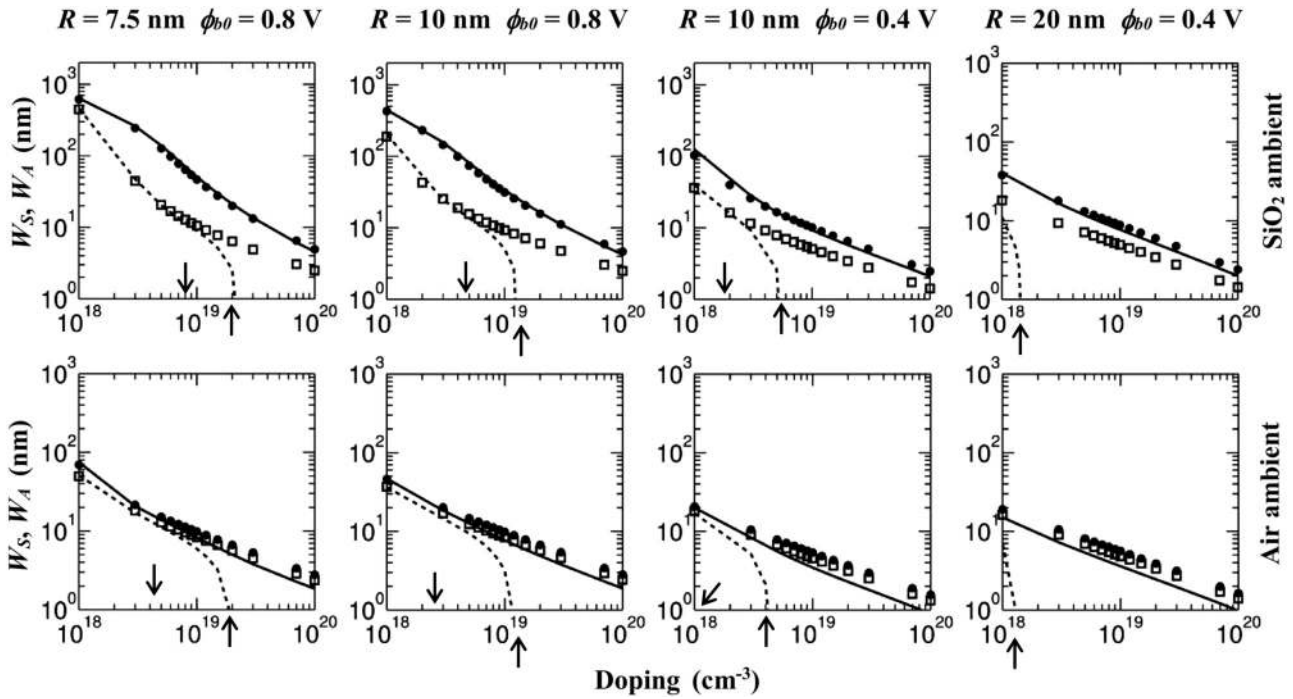

FIG. 4. Surface and axial space-charge widths—W_S and W_A as a function of doping, N_d. Lines correspond to side-bonded contact and points to end-bonded contact. The solid line and solid circles—W_S; the dashed line and open squares—W_A. Fully (partially) depleted regime lies to the left (right) of the upward arrow. End-bonded regime lies to the left of the downward arrow.

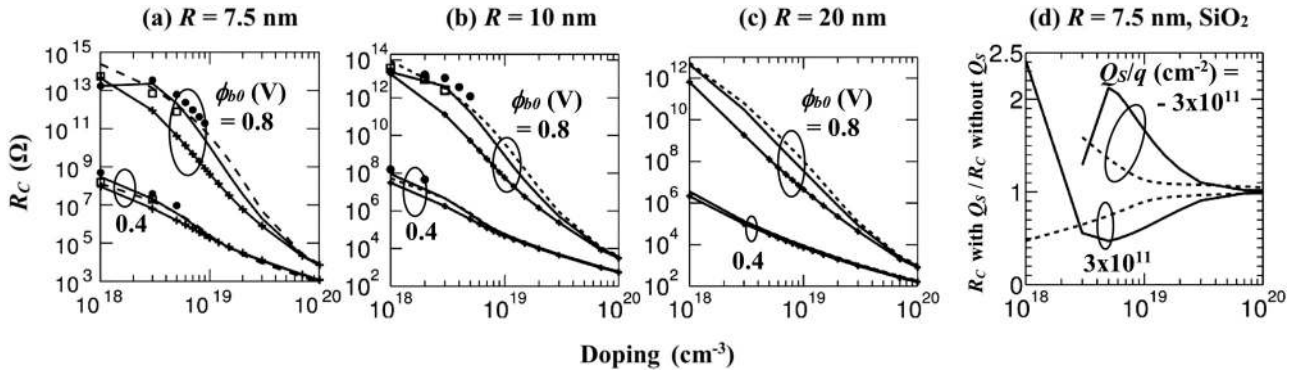

FIG. 5. (a)–(c) Contact resistance, R_C, as a function of doping, N_d. Lines correspond to side-bonded contacts; solid (starred) lines are for SiO_2(air) ambient; dashed lines represent approximate calculations which exclude all the effects other than purely radial tunneling and image force barrier lowering. In (a) and (b), points correspond to R_C of end-bonded contacts in the end-bonded regime of the side-bonded contact defined in Fig. 4; solid circles (open squares) are for SiO_2 (air) ambient. (d) The effect of Q_S on R_C of a thin NW. Solid (dashed) line is for $\phi_{b0} = 0.8$ V (0.4 V). Tunneling mass = $0.3\,m_0$ and $T = 300$ K.

However, these values may differ in the tunneling dominated portion of the end-bonded regime, e.g., for $N_d = 4 \times 10^{18}$ cm^{-3}, $R = 10$ nm, $\phi_{b0} = 0.8$ V, and SiO_2, R_C of the SBC is 8 times smaller than that of the EBC. The reason for this is as follows. Though the charge conditions near the space-charge edge are almost the same for the two contacts [see W_A, W_S in Fig. 4 or potential lines of Fig. 6(a)], deep inside, the field at the right edge of the SBC is much higher than that at the end-bonded junction [see Figs. 6(a) and 6(b)]. This increases the tunneling rate at the former location significantly [see Fig. 6(c)]. Since tunneling is sensitive to the field, the current in the SBC is higher. On the other hand, the GR current in the side-bonded contact and EBC are almost the same in the GR dominated regime, because the GR occurs in the non-contacted region a little away from the contact edge [see Fig. 6(d)]. At this location, the potential distributions in the SBC and EBC are almost the same and radially uniform [see Fig. 6(a)] causing the GR rate and hence R_C in the two contacts to resemble strongly.

In Figs. 5(a)–5(c), we compare the accurate R_C calculations with the approximate results obtained by excluding all the effects other than purely radial tunneling and image force barrier lowering. The accurate and approximate results are quite close for $\phi_{b0} = 0.4$ V, but the discrepancy between them increases with ϕ_{b0} and the following are observed at $\phi_{b0} = 0.8$ V.

- For air ambient, accurate R_C calculations can be lower by two orders of magnitude, bringing out the strong role of edge tunneling.
- A change of ambient dielectric from air to SiO_2 can increase R_C by more than an order of magnitude, bringing out the strong influence of the fringing field. Interestingly, it is this neglected field which causes the above two calculations for SiO_2 ambient to come close, by increasing the W_S, which suppresses the edge tunneling and makes the field near the right edge of the contact more radial.
- Near $N_d = 1 \times 10^{18}$ cm^{-3} and $R = 7.5$ nm, a combination of GR current and high W_S due to the fringing field are seen to lower the R_C by >1 order of magnitude.

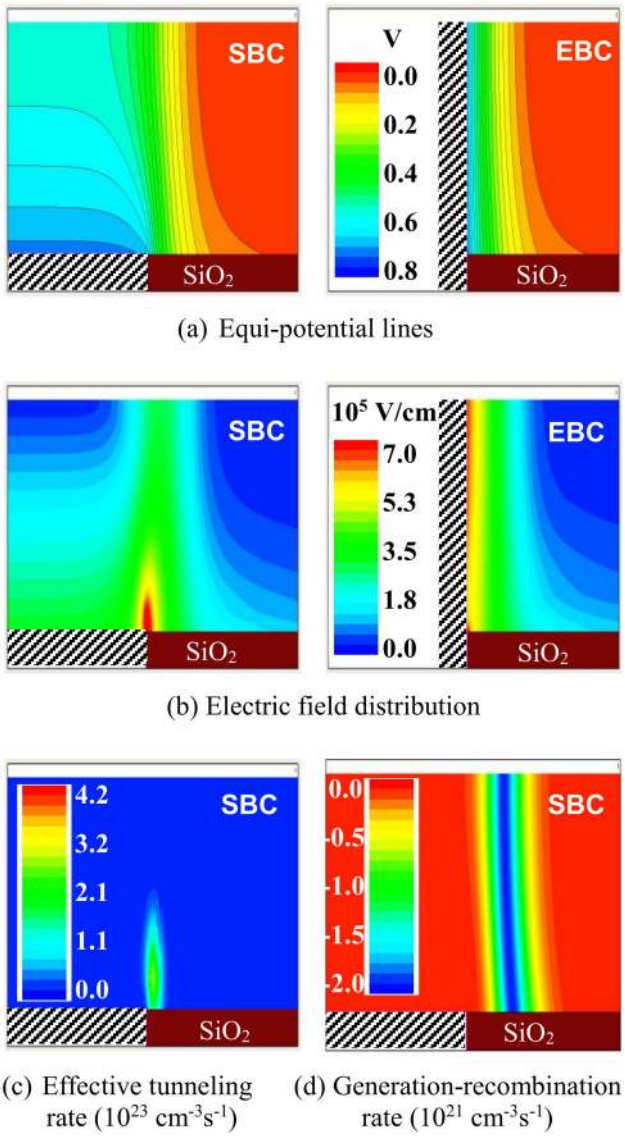

FIG. 6. Internal pictures of a side-bonded contact (SBC) and end-bonded contact (EBC) for $R = 10$ nm, $\phi_{b0} = 0.8$ V, SiO_2 ambient, tunneling mass = $0.3\,m_0$, and $T = 300$ K. Doping $N_d = 4 \times 10^{18}$ cm^{-3} in (a)–(c) and 1×10^{18} cm^{-3} in (d). Hatched areas are metal contacts.

E. Impact of surface charge and NW length

We study the impact of Q_S in contacts with $R = 7.5$ nm since this impact would be more on thinner NWs. The doping dependence of the ratio of R_C with Q_S to R_C without Q_S given in Fig. 5(d) can be explained as follows. The ratio $\rightarrow 1$ for $N_d \rightarrow 10^{20}$ cm^{-3} since heavy doping effectively screens Q_s. A +ve Q_S reduces the space charge width in an n-type NW and hence reduces tunneling dominated R_C and increases GR dominated R_C. That is why for +ve Q_S, the ratio is <1 over the tunneling dominated regimes, namely, the entire N_d range for $\phi_{b0} = 0.4$ V and $N_d > 2.5 \times 10^{18}$ cm^{-3} for $\phi_{b0} = 0.8$ V; the ratio is >1 over the GR dominated regime $N_d \leq 2.5 \times 10^{18}$ cm^{-3} for $\phi_{b0} = 0.8$ V; the shapes of the curves is a consequence of these constraints. The curves for –ve Q_S display exactly the opposite behavior.

The NW length may be as short as $L_{NW} = 100$ nm in practical contacts. Figure 4 shows that $W_S > 100$ nm in contacts with $\phi_{b0} = 0.8$ V for $R = 7.5$–10 nm and SiO_2 at lower N_d. Hence, shortening the NW to 100 nm in these contacts reduces their space-charge width. This reduces GR but raises tunneling and affects their R_C. These contacts are seen to operate in the end-bonded regime. Our calculations show that changes in their R_C are indeed along the lines of EBCs discussed in our prior work.[18] At $N_d = 10^{18}$ cm^{-3} where W_S is maximum, for SiO_2, the R_C rises by a factor of 2.2 (1.4) for $R = 7.5$ (10) nm at $\phi_{b0} = 0.8$ V where the GR current dominates and falls by a factor of 1.13 for $R = 7.5$ nm, $\phi_{b0} = 0.4$ V where the tunneling dominates. These short NW results correspond to a structure wherein on the side opposite to the metal contact, the NW (of length L_{NW}) is terminated by a wide n+ substrate (doping $= 5 \times 10^{20}$ cm^{-3}) on which the NW is realized.[18] Analysis of this simple structure can give a feel for the behavior of a NW contact which is a part of a device, e.g., contact to the ungated portion of a NW FET; in this case, other parts of the device limit the portion of the NW which can be influenced by the surrounding field from the contact.

F. Current distribution

Further insight into the operation of a SBC is gained by comparing the distribution of the axial current density, J_Z, obtained from accurate calculations with that obtained from approximate calculations wherein all the effects other than purely radial tunneling and image force barrier lowering are excluded. By way of example, Fig. 7(a) shows such calculations of J_Z along the NW axis, z, and Fig. 7(b) along the NW radial direction, r, for a contact operating in the partial depletion regime assumed in the prior model.

In Fig. 7(a), the linear variation of J_Z in the contacted region is in accordance with the prior model. This is because the prior model[9] predicts an exponentially decaying J_Z with z with a characteristic length called the transfer length, L_T, for $L_C >> L_T$; this decay becomes approximately linear for $L_C << L_T$. Indeed, purely radial tunneling simulations for $L_C = 10$ μm long contact showed an exponential decay of J_Z within the contacted region away from the contact edge with $L_T = 1.6$ μm which is $>> L_C = 200$ nm employed in Fig. 7. This agreement of our purely radial tunneling simulations with the prior model confirms the soundness of our numerical calculations.

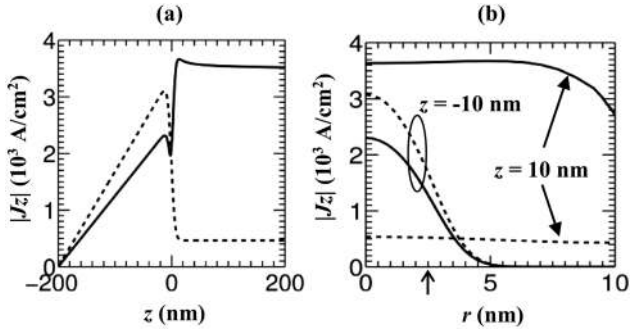

FIG. 7. Distribution of the axial current density in a tunneling dominated SBC operating in the partial depletion regime; $R = 10$ nm, $N_d = 2 \times 10^{19}$cm^{-3}, $\phi_{b0} = 0.8$ V, air ambient, tunneling mass $= 0.3\, m_0$, and $T = 300$ K. Solid line represents accurate calculations, and dashed line approximate calculations which exclude all the effects other than purely radial tunneling and image force barrier lowering. (a) Distribution along the NW axis; the contact exists for $z \leq 0$. (b) Radial distributions in the contacted and non-contacted regions; $r = 0$ represents NW axis and the upward arrow is the depletion edge as per Eq. (5).

Figures 7(a) and 7(b) show that in the non-contacted region, J_z is approximately uniform over the NW length and cross section. However, J_z is highly non-uniform over the NW cross section in the contacted region. The fact that in the contacted region the accurate J_z is lower than that in the prior model is an evidence of the propagation of the effects of the fringing field into this region. The J_Z of the prior model falls from the contacted to non-contacted region to conserve the current in the presence of an increase in the conduction area from $\pi(R - W_r)^2$ to πR^2. In contrast, the accurate J_Z increases under the same conditions due to the edge tunneling (into the non-contacted region) which is ~6 times the radial tunneling of the prior model.

IV. LIMITATIONS OF THE PRIOR MODEL

Figure 4 shows that, in an SBC, the space-charge extension into the non-contacted region is significant in all regimes of operation and can be as high as that in an EBC. The prior model neglected this effect. As regards the contacted region, the prior model based on the depletion approximation gives the potential drop for fully depleting a NW as $qN_dR^2/4\varepsilon_s$. However, we showed in Sec. III B that even when the field is purely radial, this potential drop is lower by a factor of 1.15 due to the tail in the space-charge region; this applies to the left edge of the contact [see Fig. 2(d)]. On the other hand, we showed in Sec. III C that near the right edge of the contact afflicted by space-charge curvature effects or field crowding, this potential drop is higher by a factor of $1/\alpha_{FD} = 1.37$ (1.12) for air (SiO_2) ambient.

Consider the approximate calculations of Figs. 5(a)–5(c) in the partial depletion regime defined in Fig. 4. These are obtained by excluding all the effects other than purely radial tunneling and image force barrier lowering and correspond to the prior model which assumed the SBC to be partially depleted. Based on the comparison of accurate R_C calculations with the approximate calculations given in Sec. III D,

we find that the prior model may be adequate to predict the R_C behavior for $\phi_{b0} = 0.4$ V but is significantly inaccurate at higher $\phi_{b0} = 0.8$ V. This is because the prior model neglects the edge tunneling, fringing field, and GR current. In spite of this deficiency, the prior model comes closer to the accurate calculations for SiO_2 ambient, for which one of the two effects neglected in the prior model (fringing field) suppresses the other (edge tunneling) as mentioned in Sec. III D.

In Fig. 7(b), even when the tunneling is purely radial and fringing fields are absent, the J_Z in the contacted region is seen to be non-uniform over r and encroaching significantly into the depletion width $W_r = 7.7$ nm calculated from Eq. (5). This shows that the prior model's assumption of radially uniform J_Z over the undepleted cross section which has radius $(R–W_r)$ is invalid. The J_Z encroaches into the depletion region up to the point from where the current tunnels into the contact; the distance of this point from the contact, called the tunneling distance, is known to be $<W_r$.

V. CONCLUSION

We highlighted the significant role of the edge tunneling, fringing field, and generation-recombination current, which were neglected in the prior model of a side-bonded contact. We showed that due to these effects, a side-bonded contact can operate in different regimes and can even behave like an end bonded contact under certain conditions. Furthermore, the contact resistance can reduce by up to two orders of magnitude as compared to the prior model and the space-charge can extend significantly into the non-contacted region.

[1]F. Léonard and A. A. Talin, Nat. NanoTechnol. **6**, 773 (2011).
[2]W. Li, M. D. Brubaker, B. T. Spann, K. A. Bertness, and P. Fay, IEEE Electron Device Lett. **39**, 184 (2018).
[3]S. Sett, K. Das, and A. K. Raychaudhuri, J. Appl. Phys. **121**, 124503 (2017).
[4]D. P. Tran, M. A. Winter, B. Wolfrum, R. Stockmann, C. T. Yang, M. P. Moghaddam, A. Offenhäusser, and B. Thierry, ACS Nano **10**, 2357 (2016).
[5]M. Berg, J. Svensson, E. Lind, and L.-E. Wernersson, Appl. Phys. Lett. **107**, 232102 (2015).
[6]Y. Calahorra, E. Yalon, and D. Ritter, J. Appl. Phys. **117**, 034308 (2015).
[7]Y. Zhai, L. Mathew, R. Rao, M. Palard, S. Chopra, J. G. Ekerdt, L. F. Register, and S. K. Banerjee, IEEE Trans. Electron Devices **61**, 3896 (2014).
[8]E. Stern, G. Cheng, M. P. Young, and M. A. Reed, Appl. Phys. Lett. **88**, 053106 (2006).
[9]S. E. Mohney, Y. Wang, M. A. Cabassi, K. K. Lew, S. Dey, J. M. Redwing, and T. S. Mayer, Solid-State Electron. **49**, 227 (2005).
[10]H. Park, R. Beresford, S. Hong, and J. Xu, J. Appl. Phys. **108**, 094308 (2010).
[11]Z. R. Wang, G. Zhang, K. L. Pey, C. H. Tung, and G. Q. Lo, J. Appl. Phys. **105**, 094508 (2009).
[12]F. Léonard and A. A. Talin, Phys. Rev. Lett. **97**, 026804 (2006).
[13]A. A. Shukkoor and S. Karmalkar, J. Appl. Phys. **122**, 214501 (2017).
[14]C. Fernandes, A. Shik, K. Byrne, D. Lynall, M. Blumin, I. Savaliev, and H. E. Ruda, Nanotechnology **26**, 085204 (2015).
[15]X. L. Han, G. Larrier, E. Dubois, and F. Cristiano, Surf. Sci. **606**, 836 (2012).
[16]F. Léonard, A. A. Talin, B. Swartzentruber, and S. Picraux, Phys. Rev. Lett. **102**, 106805 (2009).
[17]A. Chaudhry, V. Ramamurthi, E. Fong, and M. Saif Islam, Nano Lett. **7**, 1536 (2007).
[18]A. A. Shukkoor and S. Karmalkar, J. Appl. Phys. **124**, 084502 (2018).
[19]S. M. Sze and K. K. Ng, *Physics of Semiconductor Devices* (Wiley India, New Delhi, 2007).
[20]A. Y. C. Yu, Solid-State Electron. **13**, 239 (1970).
[21]C. Y. Chang, Y. K. Fang, and S. M. Sze, Solid-State Electron. **14**, 541 (1971).
[22]S. Zhu, J. Chen, M. F. Li, S. J. Lee, J. Singh, C. X. Zhu, A. Du, C. H. Tung, A. Chin, and D. L. Kwong, IEEE Electron Device Lett. **25**, 565 (2004).
[23]M. Jang, Y. Kim, J. Shin, and S. Lee, IEEE Electron Device Lett. **26**, 354 (2005).
[24]N. Stavitski, M. J. H. van Dal, A. Lauwers, C. Vrancken, A. Y. Kovalgin, and R. A. M. Wolters, IEEE Electron Device Lett. **29**, 378 (2008).
[25]J. Hu, Y. Liu, C. Z. Ning, R. Dutton, and S. M. Kang, Appl. Phys. Lett. **92**, 083503 (2008).
[26]V. Schmidt, J. V. Wittemann, S. Senz, and U. Gösele, Adv. Mater. **21**, 2681 (2009).
[27]L. Li, Y. Fang, C. Xu, Y. Zhao, N. Zang, P. Jiang, and K. J. Ziegler, Nanotechnology **27**, 165303 (2016).
[28]S. A. Dayeh, R. Chen, Y. G. Ro, and J. Sim, Mater. Sci. Semicond. Process. **62**, 135 (2017).
[29]H. Schmid, M. T. Bjork, J. Knoch, S. Karg, H. Riel, and W. Riess, Nano Lett. **9**, 173 (2009).
[30]V. Schmidt, S. Senz, and U. Gösele, Appl. Phys. A **86**, 187 (2007).
[31]I. Kimukin, M. S. Islam, and R. S. Williams, Nanotechnology **17**, S240 (2006).
[32]K. Seo, S. Sharma, A. A. Yasseri, D. R. Stewart, and T. I. Kamins, Electrochem. Solid State Lett. **9**, G69 (2006).
[33]K. K. Ng and R. Liu, IEEE Trans. Electron Devices **37**, 1535 (1990).
[34]V. K. Gurugubelli and S. Karmalkar, J. Appl. Phys. **119**, 024507 (2016).
[35]M. Ribeiro, Jr., J. Appl. Phys. **117**, 234302 (2015).
[36]C. T. Sah, *Fundamentals of Solid State Electronics* (World Scientific, Singapore, 1991).
[37]Y. M. Niquet, A. Lherbier, N. H. Quang, M. V. Fernandes-Serre, X. Blase, and C. Delerue, Phys. Rev. B **73**, 165319 (2006).
[38]M. Diarra, Y. M. Niquet, C. Delerue, and G. Allan, Phys. Rev. B **75**, 045301 (2007).
[39]S. M. Wong, H. Y. Yu, J. S. Li, Y. L. Li, N. Singh, P. G. Q. Lo, and D. L. Kwong, IEEE Electron Device Lett. **32**, 176 (2011).
[40]*Sentaurus Device User Guide* (Synopsys, 2015).
[41]R. M. Corless, G. H. Gonnet, D. E. G. Hare, D. J. Jeffrey, and D. E. Knuth, Adv. Comput. Math. **5**, 329 (1996).